Low-dimensional In2O3 nanostructures on MgO cubes

Jacek Goniakowski, Cédric Baumier, F. Fortuna, Slavica Stankic

ARTICLE

Low-dimensional In_2O_3 nanostructures on MgO cubes

Jacek Goniakowski,*[a] Cédric Baumier[b], Franck Fortuna[c] and Slavica Stankic*[a]

Received 00th January 20xx,
Accepted 00th January 20xx

DOI: 10.1039/x0xx00000x

We report a successful synthesis of low-dimensional In_2O_3 nanostructures on MgO smoke particles using an innovative fabrication method. By co-combusting indium and magnesium in an oxygen-rich atmosphere, the energy released (heat) upon oxidation of Mg provides the conditions for the simultaneous evaporation of In resulting in the self-organized growth of indium oxide particles with consistent orientation. Notably, we report the stabilization of the typically unstable trigonal In_2O_3 polymorph on edges and corners of MgO cubes. These experimental results align well with the energetics extracted from atomistic models, which offers valuable insights into the thermodynamic factors driving the In_2O_3 stabilization on such less dense MgO terminations. This work marks a significant advancement in multi-metal oxide (MMO) research and nanostructure engineering.

Introduction

Metal oxides can be optimized for specific applications or reactions by strategically combining two metals within a single oxide compound. Multi-metal oxides (MMOs) are materials that exhibit enhanced performance, stability, and customizable properties, often surpassing the capabilities of their individual metal oxide counterparts. A great multitude of variations stems from the number of possible metal combinations, which makes them easily tuneable to serve specific applications. The versatility of MMOs extends their usefulness across various fields, including catalysis, organic synthesis and fine chemical production, energy storage and conversion (such as in batteries and supercapacitors), environmental remediation, electronics, sensors, and more.[1-5] By incorporating cations of different sizes, electronegativities, and reducibilities, one can fine-tune the surface structure and composition, electronic characteristics, and reactivity of these materials.[6]

The properties of MMOs are further influenced by their low dimensionality, which allows for greater flexibility in stoichiometry, atomic structure, and electronic characteristics as the material size decreases. This often leads to the formation of complex compounds with no bulk equivalents. Indeed, at the nanoscale, some thermodynamically unfavourable polymorphs may be stabilized, or entirely new structures may emerge.[7] Moreover, phenomena such as mixing, phase separation, solid solution formation, and surface segregation determine MMO's characteristics.[8] In particular, the presence of a second metal or metal oxide may significantly affect the relative surface stabilities, resulting in particle shapes and morphologies that deviate from expectations and leading to unexpected segregation.[9] This can be crucial for surface (photo-)chemical activity, thereby broadening the material's potential applications as illustrated by a remarkable transformation in the dispersion of In_2O_3 catalyst during the water gas shift reaction.[10] Initially present as free nanoparticles, the In_2O_3 catalyst was observed to reorganize into nanolayers that covered the surface of the TiO_2 host material. This finding is particularly noteworthy as it demonstrates the interface confinement effect in oxide/oxide catalytic systems.

Magnesium oxide (MgO) is a stable ionic compound with a cubic crystal structure and minimal chemical reactivity, which has been frequently used as a substrate for the epitaxial growth of In_2O_3 thin films.[11,12] The excellent lattice matching between MgO and In2O3 facilitates the growth of high-quality epitaxial films, which are crucial for various electronic and optoelectronic devices.[13,14] The combination of In_2O_3 and MgO has been also explored in the context of crystal defect formation and doping. For example, Niedermaier and colleagues studied the effects of admixing trivalent In^{3+} ions into the MgO host lattice, uncovering insights into grain growth, morphology evolution, and impurity segregation.[15]

At the nanoscale, MgO has been widely employed to stabilize either metals or other oxide particles on its surfaces. Oxides that adopt the same cubic structure (e.g., CaO, SrO, BaO) have been combined with nano-MgO, leading to the creation of photoluminescent compounds with novel optical properties.[16] When mixed with Zn, the resulting $Zn_xMg_{1-x}O$ nanostructures displayed tuneable surface, optical, and biological activities.[17-19] In these nanostructures, the stabilization of the otherwise unstable cubic ZnO polymorph on the MgO support opened up new avenues for crystal structure engineering, that could be particularly useful in applications like hydrogen storage.

MgO smoke has been shown to be an ideal model for exploring particle morphology on complex geometries and confined sites. [20] The co-evaporation of silver during MgO smoke formation, for instance, revealed that sites on the MgO surface, such as flat (100) surfaces, stepped surfaces, and

[a] CNRS UMR 7588, Sorbonne Université, Institut des NanoSciences de Paris (INSP), 4 place Jussieu, 75252 Paris cedex 05, France.
[b] CNRS UMR 9012, Université Paris-Saclay, Laboratory of the Physics of the two Infinities Irène Joliot-Curie (IJCLab), Orsay Cedex 91405, France.
[c] CNRS UMR8214, Université Paris-Saclay, Institut des Sciences Moléculaires d'Orsay (ISMO), Bât 520, Orsay Cedex 91405, France.
† Footnotes relating to the title and/or authors should appear here.

contact lines between MgO cubes, play a significant role for the nucleation behaviour. In this context, we report herein a combined experimental and theoretical study on low-dimensional In_2O_3 particles uniformly and equidistantly distributed along the edges and corners of MgO smoke. Stabilization of the uncommon trigonal In_2O_3 polymorph as well as its unique growth orientation on MgO smoke cubes, makes this system a promising model with several questions to be further resolved.

Experimental and theoretical methods

Synthesis and characterization

A co-combustion engaged synthesis was employed to obtain low-dimensional In_2O_3 on MgO cubes. Pure MgO smoke powders were synthesized in a home-made glove box by burning magnesium foil (Goodfellow, purity 99.9%) in air. For the purpose of In-based powder synthesis, the Mg foil was wrapped with In wires (Goodfellow, purity 99.99%) in such a way that In could be evaporated during Mg combustion. The powders were collected on a glass plate that was kept at a constant height (10 cm) above the sampling point, allowing the collection of particles near the generation zone. The powders were collected straight after the combustion process and kept in high vacuum ($P < 10^{-5}$ mbar) prior to any investigation in order to avoid any interaction/ contamination by air. TEM analysis was performed on two types of microscopes: (a) Tecnai G2 20 Twin accelerating voltage 200 kV, with spatial resolution 0,27 nm, scanning transmission resolution 0,08 nm (at 200 kV), spherical aberration coefficient 2,0 mm and magnification ranges 70 to 700 000. The microscope is equipped with a high-resolution camera (4k×4k- Gatan OneView in situ) an EDX (Energy Dispersive X-ray spectrometer), a Scanning Transmission Electron Microscope (STEM) mode with bright and dark field detectors; (b) Thermo Fisher Titan Themis 300 transmission electron microscope, using an accelerating voltage of 300 kV. Images were recorded using the low electron dose system (10 electrons per $Å^2$ per s), with a magnification range from 20,000× to 60,000× on a Falcon 3 Direct Detection Electron 4Kx4K camera in the linear mode.

TEM grids were directly inserted into the powder samples for analysis. Measurements were conducted on the dry specimens without dissolving or suspending them in any organic solvents or additional solutions. This approach preserved the original state of the powders, ensuring that the observed structures were representative of the unaltered material. The particle size distributions were measured from TEM, by exploiting more than 150 images.

DFT simulations

All computational results were obtained within the plane waves density functional approach, using the spin-polarized gradient-corrected PW91 exchange-correlation functional[21] and the projector augmented wave method[22,23] implemented in VASP. [24,25] Indium (including 4d electrons), magnesium (including 2p electrons), and oxygen pseudopotentials provided with VASP were used. With these settings, calculated lattice parameters of bulk rocksalt MgO and bixbyite In_2O_3 are equal to a_{MgO} = 4.26 Å and a_{In2O3} = 10.29 Å, respectively. The trigonal In_2O_3 phase is predicted to be 0.15 eV/In_2O_3 less stable than the bixbyite one.

The MgO substrates were represented by (001), (011), and (111) oriented slabs composed of 4, 5, and 6 atomic layers, respectively. Indium oxide films were deposited on top sides of the slabs and the atomic coordinates of all atoms were allowed to relax until forces dropped below 0.01 eV $Å^{-1}$, apart from the bottom-most slab layers which were kept in their bulk position. For the three orientations, rectangular surface unit cells of dimensions close to those of the calculated R-cut trigonal In_2O_3 (17.63 Å x 5.58 Å) were systematically used. Their dimensions are equal to a_{MgO} √2 (3 x 1), a_{MgO} (4 x √2), and a_{MgO} √2 (1.5√3 x 1), respectively. Their Brillouin zones were sampled on the (1 x 3) Monkhorst-Pack mesh.

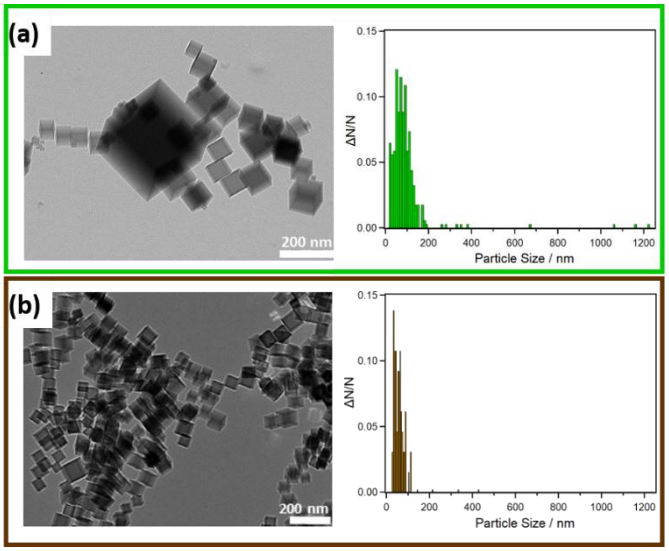

Results and discussion

Figure 1. TEM images and particle's size distribution of pure MgO smoke (a) and In_2O_3/MgO (b).

Figure 1(a) presents the TEM image and particle size distribution (PSD) of MgO smoke obtained by burning Mg in air. Consistent with previous observations,[26] MgO particles exhibit an exceptionally regular cubic shape, and the powder is polydisperse. The PSD reveals a broad range of sizes, with the majority falling between 30 nm and 150 nm. When indium is co-evaporated, the resulting particles maintain their cubic shape but become visibly smaller with a narrower size distribution (Fig. 1(b)). In this powder, the average edge length measures around 30-40 nm. In contrast to pure MgO, where a noticeable fraction of particles can reach up to ~1300 nm, the indium-containing particles do not exceed 500 nm in size. A closer inspection of the TEM image in Figure 2(a) reveals decoration patches on the MgO surface, which appear to be strongly dependent on the size of the MgO particles. Small MgO cubes show decorations only at the corners, whereas the edges of larger cubes provide sufficient space to accommodate

additional precipitates. This phenomenon is clearly illustrated in Figures 2(b) and 2(d), which show a 500 nm decorated MgO cube and its magnified view, respectively. These images further demonstrate that the precipitates display a flat shape and are uniformly and almost equidistantly (8-12 nm) distributed along the edges. Dark field TEM of the same MgO cube, obtained by selecting the [-11-2] orientation of the reciprocal space (Fig. 2(c)), confirms the presence of precipitates on the edges and corners. It also implies that all precipitates were grown with the same orientation. Notably, regardless of the TEM mode used, no precipitates were observed on the (100) MgO facets. To determine the chemical nature of the precipitates – specifically, whether they are metallic or oxidized indium – STEM and corresponding EDX mapping have been performed. The results shown in Figure 3 reveal that the layers of higher z-contrast are indium rich – more precisely identified as In_2O_3. The HRTEM presented in Figure 4(a) is representative of the orientation of the nano-precipitates growing on the corners and edges of (100) faceted MgO cubes. The corresponding diffraction pattern shown in the inset of this figure reveals a monocrystalline structure with an interplanar d-spacing of ~2.8 Å and a characteristic angle of 93° between the planes. These measurements match perfectly with the simulated pattern of the [241] direction for the trigonal In_2O_3 polymorph.

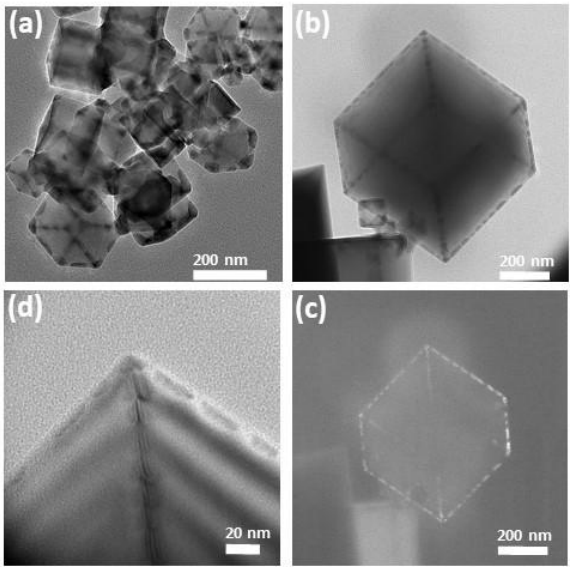

Figure 2. TEM images of In_2O_3/MgO showing the most representative particles (a), large MgO cube with regularly distributed In_2O_3 precipitates at the edges (b). Dark field TEM image of the same cube is shown in (c) and its closer inspection in (d). The dark field image was taken with a rotation of 55,44° and a tilt of 0,960° in the conical coordinate that is selecting the indium spot.

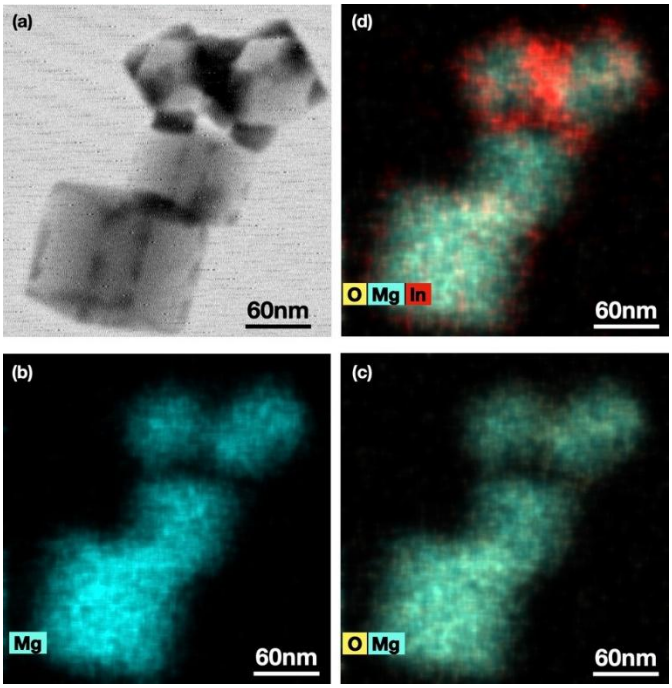

Figure 3. STEM image (a) and corresponding EDX mapping for Mg (b); MgO (c) and MgOIn (d) showing that the layers of higher z-contrast are indium rich.

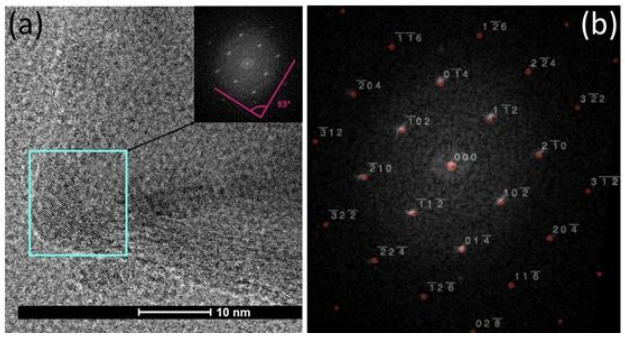

Figure 4. HRTEM image (a) and corresponding diffraction pattern orientation (inset), representative of the In-based precipitate sitting at the corner of MgO cube. Simulated diffraction pattern of [241] direction for trigonal In_2O_3 (b).

In summary, according to EDX-STEM experiments (Figure 3) the observed low-dimensional In-based precipitates on MgO cubes are composed of indium oxide. These precipitates grow with a consistent orientation on the low-coordination sites at edges and corners of MgO cubes. Most surprisingly, these In_2O_3 precipitates on the MgO surface adopt the thermodynamically less stable bulk In_2O_3 phase, specifically the trigonal, corundum-like structure. This finding contrasts with the alternative synthesis route proposed by Niedermaier et al., [15] where In_2O_3 in the cubic bixbyite structure was reported to form upon annealing of In-doped MgO powders (c_{In}=10 at %) at temperatures between 873 K and 1173 K. It's worth noting that a minor fraction of metastable

rhombohedral In_2O_3 has been successfully stabilized on the (0001) surface of α-Al2O3.[27] This stabilization was attributed to the complementary bonding symmetries between the two oxide structures. In that case, the epitaxial relationship was maintained through a precise matching of lattice planes at the interface.

In order to rationalize these observations, we will report and discuss results of DFT calculations on a series of InO_x/MgO systems. Following the firm experimental indication of the formation of low-dimensional trigonal In_2O_3 precipitates selectively at edges and corners of MgO cubes, and in absence of precise experimental characterization necessary to construct their atomistic models, we will focus on the site-dependence of interactions between the two oxides with help of three low-index MgO surfaces: (100), (110), and (111). These surfaces, with 5-, 4-, and 3-fold coordinated surface sites, respectively, mimic the local environments of ions at faces, edges, and corners of ideal MgO cubes. In the following, in three complementary steps we will characterize: (a) segregation of isolated In substitutions, (b) wetting by a monolayer-thick In_2O_3 film, and (c) adhesion at a constituted In_2O_3/MgO interface.

We first examine the behaviour of isolated In atoms substituting Mg cations in the perfect MgO lattice, a scenario likely occurring during the experimental powder synthesis via co-combustion of Mg and In. Our computational findings reveal a clear preference for In substitutions to segregate to surface MgO sites. The calculated segregation energies (energy changes when moving an In substitution from bulk MgO to its surface) are equal to -2.2, -3.2, -3.8 eV/In, for the three MgO surfaces, respectively.

The negative values indicate an energy gain upon In segregation, with lower-coordinated surface sites exhibiting greater energy gains. These results suggest a lower energy cost of undercoordinated In cations compared to the Mg ones. This segregation force is additionally enhanced by elastic effects induced by the systematically longer In-O bonds which, due to steric repulsion, render bulk In substitutions strongly energetically unfavourable. A part of the strain is released upon In segregation and the release is more efficient at more open surfaces. Consequently, thermodynamics of In segregation alone drives the initial In accumulation at lower-coordinated sites of MgO cubes, and may be at the very origin of the observed In_2O_3 formation preferentially at edges and corners of the MgO cubes. Interestingly, a very similar trend (segregation energies equal to -1.0, -1.8, and -2.5 eV/$InO_{0.5}$, respectively) is obtained for segregation of a charge neutral In_2O complex (two In substitutions linked by an interstitial oxygen atom) which, in contrast to isolated In substitutions, does not involve In cations in a less favoured +2 oxidation state.

In a second step we examine the relative stability of monolayer-thick In_2O_3 films on the three MgO surfaces, which may serve as precursors to formation of constituted indium oxide precipitates. Optimized monolayers, Figure 5 (a-c), yield formation energies of +1.7, 0.0, and -0.1 eV/In_2O_3 (with respect to the bulk bixbyite In_2O_3) on MgO (100), (110), and (111) surfaces, respectively. These results indicate a clear preference for film formation on the more open MgO surfaces, and especially on the (111) one. Steric effects play an important role at this stage too. On the more open (110) and (111) surfaces, the In_2O_3 monolayers prolong the MgO lattice, thus saturating all broken surface Mg-O bonds and providing a quasi-six-fold coordination to In cations. Such favourable film structure is hindered on the MgO(100) surface due to quite distinct Mg-O and In-O bond lengths. Beyond the relative stability of the three monolayers, positive formation energy on MgO(100) suggests a thermodynamic preference for bulk-like 3D indium oxide precipitates. In contrast, zero and slightly negative energies on MgO(110) and MgO(111) indicate the possibility of a particularly stable wetting layer, prerequisite for a strongly adhering oxide film. Consequently, thermodynamics of the initial stages of oxide formation points towards quite distinct behaviour at the three MgO surfaces: a clear preference for formation of a stable In_2O_3 ultrathin film on more open MgO surfaces and its instability at the MgO(100) one. These calculated energetic characteristics are again consistent with the observed In_2O_3 formation uniquely at edges and corners of the MgO cubes.

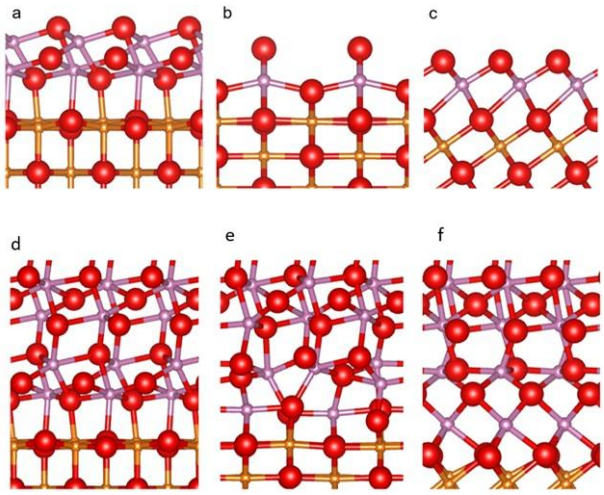

Figure 5. Atomic structure of 1ML In_2O_3 film deposited on the MgO (a) (001), (b) (110), and (c) (111) surfaces. Atomic structure of the interfacial region of the 5ML In_2O_3 film deposited on the MgO (d) (001), (e) (110), and (f) (111) surfaces. Golden, mauve, and red balls represent Mg, In, and O atoms, respectively.

In a final step, we examine the interfaces formed between the two oxides. Following the experimental indications of a corundum-structured flat indium oxide particles, we chose to systematically deposit a 5 ML-thick, corundum-structured, R-cut In_2O_3 film on the three MgO surfaces. Thanks to a relatively favourable lattice coincidence, such film can match the three

MgO surfaces with only quite minor in-plane lattice adjustments. The calculated separation energies (not including the energy cost of the lateral lattice adjustments), are 0.9, 1.8, and 2.9 J/m² for the three interface orientations, respectively. Unsurprisingly, the interface strength increases as the coordination of surface MgO ions decreases, making the (111)-orientated interface by far the most adhesive. Similarly to the behaviour predicted above for In_2O_3 monolayers, a favourably high density of Mg-O and O-In bonds at the more open MgO(110) and MgO(111) interfaces (Figure 5 (d-e)) is enabled by more efficient strain accommodation through atomic relaxations perpendicular to the interface. The calculated separation energies provide valuable estimates of interface adhesion (W) and can be compared to the surface energy of the R-cut In_2O_3 surface (σ = 1.3 J m^{-2}). Using the Kaischew-Winterbottom construction[28,29] to estimate equilibrium shapes of supported oxide precipitates ($\Delta h/h = W/\sigma$, where h denotes the height of crystal face parallel to the substrate and Δh is its reduction associated with substrate-induced shape truncation) we predict distinct wetting behaviours for the three different MgO surface orientations. At the MgO(100) surface wetting is poor ($\Delta h/h < 1$), such that formation of 3D-shaped In_2O_3 precipitates is expected. In contrast, good wetting predicted for the MgO(111) surface ($\Delta h/h \sim 2.0$), points towards formation of 2D-shaped precipitates. The MgO(110) case displays intermediate wetting characteristics, with $\Delta h/h \sim 1.5$. However, in this case, our results suggest that the strongly adhesive first In_2O_3 layer may not be fully compatible with the R-cut corundum structure and that further structural optimization of the interfacial region could potentially yield even more adhesive and stable interfaces. These results show that distinct interface energetics leads to qualitatively different equilibrium shapes of In_2O_3 precipitates on the three MgO surfaces, ranging from weakly-adhesive 3D-shaped In_2O_3 clusters on the MgO(100) surface to strongly-adhesive 2D precipitates on the (111) one. Since these predictions corroborate with the observed absence of precipitates on the facets of MgO cubes and with the presence of 2D-shaped ones at cube edges and corners, they provide valuable first insights into the thermodynamic bias behind the growth behaviour of In_2O_3 on MgO.

The calculated thermodynamic trends discussed above may be sensitive to a more precise account for the atomic structure at the interface, including factors such as the exact precipitate thickness, the precise morphology of MgO edges and corners, an oxygen excess/deficiency, or cationic mixing at the interface. However, other physical effects could play a crucial role in the formation of the observed precipitates. On one hand, the kinetics of indium segregation, oxidation, and surface diffusion might determine the most likely sites for precipitate formation and could explain the observed organization of precipitates along cube edges. On the other hand, this organization might also be influenced by long-range elastic effects within the MgO particles. Finally, the smaller size of In_2O_3/MgO cubes (Fig. 1b) may be due to two potential factors. First, an In_2O_3 layer could inhibit the growth of MgO cubes by acting as a protective barrier. Alternatively, indium might influence MgO nucleation, promoting the formation of more numerous, smaller nuclei.

Conclusions

In conclusion, we have demonstrated an innovative synthesis approach in which the energy released (heat) upon oxidation of one metal (Mg) provides the conditions for the simultaneous evaporation of a second metal (In), resulting in the formation of multi-metal oxide nanostructures (In_2O_3/MgO). Through this method, we have successfully synthesized site-selective, low-dimensional In_2O_3 nanostructures on MgO smoke particles. These nanostructures exhibit several remarkable properties including remarkable self-organization, an otherwise unstable trigonal crystal structure and a strong epitaxial relationship with the MgO substrate. Our computational analysis confirms excellent In segregation and In_2O_3 wetting characteristics on the MgO(111) and MgO(110) surfaces, indicating a high propensity for 2D-shaped precipitate formation at the edges and corners of MgO cubes. In contrast, both these characteristics are much less favourable at the MgO(100) surface, which aligns with the observed absence of In_2O_3 precipitates on the cube facets. The unique characteristics of the In_2O_3-MgO couple among metal-metal oxide (MMO) systems open several avenues for further research, including a detailed examination of the In_2O_3-MgO interface(s) and analysis of mechanisms behind the self-organization of In_2O_3 precipitates along cube edges. These insights not only enhance our understanding of oxide nanostructure formation but also open new possibilities in nanotechnology and materials science.

Author contributions

The manuscript was written through contributions of all authors. All authors have given approval to the final version of the manuscript.

Conflicts of interest

There are no conflicts to declare.

Data availability

The data supporting the findings of this study are available upon request.

Acknowledgements

The authors are thankful to Eric Larquet from Laboratoire de Physique des Interfaces et des Couches Minces (LPIMC) for HRTEM measurements. We are also grateful to Dominique Demaille from Institut des NanoSciences de Paris (INSP-CNRS-

Sorbonne University) and Nicolas Menguy from Institut de minéralogie, de physique des matériaux et de cosmochimie (IMPMC-Sorbone University) for fruitful discussions regarding the interpretations of (HR)TEM results.

Notes and references

1 X. Ma, J. S. A. Carneiro, X. K. Gu, H. Qin, H. Xin, K. Sun and E. Nikolla, ACS Catal., 2015, 5, 4013–4019.
2 K. Ramany, R. Shankararajan, K. Savarimuthu, S. Venkatachalapathi, G. Sivakumar, D. Murali and I. Gunasekaran, Mater. Lett., 2021, 301, 130248–130259.
3 J. Kim, W. Ko, J. M. Yoo, V. K. Paidi, H. Y. Jang, M. Shepit, J. Lee, H. Chang, H. S. Lee, J. Jo, B. H. Kim, S. P. Cho, J. van Lierop, D. Kim, K. S. Lee, S. Back, Y. E. Sung and T. Hyeon, Adv. Mater., 2022, 34, 2107868.
4 Y. Chen, Y. Miao, X. Hu, D. Kim, Y. Zhu, Y. Su, Y. Fan, H. Qiao, B. Yu and Y. I. Chen, Energy Storage Mater., 2023, 63, 102989.
5 E. Sartoretti, C. Novara, M. C. Paganini, M. Chiesa, M. Castellino, F. Giorgis, M. Piumetti, S. Bensaid, D. Fino and N. Russo, Catal. Today, 2023, 420, 114037.
6 W. Huang, J. Zhang, D. Liu, W. Xu, Y. Wang, J. Yao, H. T. Tag, K. N. Dinh, C. Wu, M. Kuang, W. Fang, R. Dangol, L. Song, K. Zhou, C. Liu, J. W. Xu, B. Liu and Q. Yan, ACS Nano, 2020, 14, 17640–17651.
7 G. Wilde, Adv. Eng. Mater., 2021, 23, 2001387.
8 F. P. Netzer and C. Noguera, Oxide Thin Films and Nanostructures, Oxford University Press, 2021.
9 R. Lin, E. Hu, M. Liu, Y. Wang, H. Cheng, J. Wu, J. C. Zheng, Q. Wu, S. Bak, X. Tong, R. Zhang, W. Yang, K. A. Persson, X. Yu, X. Q. Yang and H. L. Xin, Nat. Commun., 2019, 10, 1650.
10 J. Wang, R. Li, G. Zhang, C. Dong, Y. Fan, S. Yang, M. Chen, X. Guo, R. Mu, Y. Ning, M. Li, Q. Fu and X. Bao, J. Am. Chem. Soc., 2024, 146, 5523–5531.
11 Z. Li, C. Zhao, W. Mi, C. Luan, X. Feng and J. Ma, Ceram. Int., 2014, 40, 4203–4206.
12 X. Du, J. Yu, X. Xiu, Q. Sun, W. Tang and B. Man, Vacuum, 2019, 167, 1–5.
13 C. K. Nguyen, A. Mazumder, E. L. H. Mayes, V. Krishnamurthi, A. Zavabeti, B. J. Murdoch, X. Guo, P. Aukarasereenont, A. Dubey, A. Jannat, X. Wei, K. V. Truong, L. Bao, A. Roberts, C. F. McConville, S. Walia, N. Syed and T. Daeneke, Adv. Mater. Interfaces, 2023, 10, 2202036–2202044.
14 B. K. Yap, Z. Zhang, G. S. H. Thien, K. Y. Chan and C. Y. Tan, Appl. Surf. Sci. Adv., 2023, 16, 100423.
15 M. Niedermaier, C. Taniteerawong, T. Schwab, G. Zickler, J. Bernardi and O. Diwald, ChemNanoMat, 2019, 5, 634–641.
16 A. Sternig, S. Stankic, M. Müller, J. Bernardi, E. Knözinger and O. Diwald, Adv. Mater., 2008, 20, 4840–4844.
17 S. Stankic, A. Sternig, F. Finocchi, J. Bernardi and O. Diwald, Nanotechnology, 2010, 21, 355603.
18 F. Haque, F. Finocchi, S. Chenot, J. Jupille and S. Stankic, J. Phys. Chem. C, 2021, 125, 25841–25850.
19 S. Auger, C. Henry, C. Péchoux, S. Suman, N. Lejal, N. Bertho, T. Larcher, S. Stankic and V. Vidic, Sci. Rep., 2018, 8, 12276.
20 S. Stankic, R. Cortes-Huerto, N. Crivat, D. Demaille, J. Goniakowski and J. Jupille, Nanoscale, 2013, 5, 2448.
21 J. P. Perdew and Y. Wang, Phys. Rev. B, 1992, 45, 13244–13249.
22 P. E. Blöchl, Phys. Rev. B, 1994, 50, 17953–17979.
23 G. Kresse and D. Joubert, Phys. Rev. B, 1999, 59, 1758–1775.
24 G. Kresse and J. Furthmüller, Phys. Rev. B, 1996, 54, 11169–11186.
25 G. Kresse and J. Hafner, Phys. Rev. B, 1993, 47, 558–561.
26 S. Stankic, M. Cottura, D. Demaille, C. Noguera and J. Jupille, J. Cryst. Growth, 2011, 329, 52–56.
27 K. H. L. Zhang, V. K. Lazarov, P. L. Galindo, F. E. Oropeza, D. J. Payne, H. H.-C. Lai and R. G. Egdell, Cryst. Growth Des., 2012, 12, 1000–1007.
28 R. Kaischew, Arbeitstagung Festkörper Physik, Dresden: Verlag, 1952, 81.
29 W. L. Winterbottom, Acta Metall., 1967, 15, 303.